Available online at www.sciencedirect.com

SCIENCE @ DIRECT®

International Journal of Heat and Mass Transfer 47 (2004) 4177–4193

International Journal of HEAT and MASS TRANSFER

www.elsevier.com/locate/ijhmt

Constructal flow structure for a PEM fuel cell

J.V.C. Vargas [a,*], J.C. Ordonez [b], A. Bejan [c]

[a] *Departamento de Engenharia Mecânica, Universidade Federal do Paraná, C.P. 19011, Curitiba, Paraná 81531-990, Brazil*
[b] *Department of Mechanical Engineering and Center for Advanced Power Systems, Florida State University, Tallahassee, FL 32310-6046, USA*
[c] *Department of Mechanical Engineering and Materials Science, Duke University, Durham, NC 27708-0300, USA*

Received 15 March 2004; received in revised form 6 May 2004

Abstract

This paper introduces a model and a structured procedure to optimize the internal structure (relative sizes, spacings) and external shape (aspect ratios) of a unit PEM fuel cell so that net power is maximized. The optimization of flow geometry is conducted for the smallest (elemental) level of a fuel cell stack, i.e., the unit PEM fuel cell, which is modeled as a unidirectional flow system. The polarization curve, total and net power, and efficiency are obtained as functions of temperature, pressure, geometry and operating parameters. The optimization is subjected to fixed total volume. There are two levels of optimization: (i) the internal structure, which basically accounts for the relative thicknesses of two reaction and diffusion layers and the membrane space, and (ii) the external shape, which accounts for the external aspect ratios of a square section plate that contains all unit PEM fuel cell components. The available volume is distributed optimally through the system so that the net power is maximized. Temperature and pressure gradients play important role, especially as the fuel and oxidant flow paths increase. Numerical results show that the optimized internal structure is "robust" with respect to changes in external shape. The optimized internal structure and external shape are a result of an optimal balance between electrical power output and pumping power required to supply fuel and oxidant to the fuel cell through the gas channels. Directions for future improvements at the PEM fuel cell stack level in flow architecture (constructal design) are discussed.

Keywords: Constructal PEM fuel cells; Internal structure; External shape

---

1. Introduction

Fuel cell technology is well advanced, with applications in stationary power generation and in vehicles [1–4]. Proton exchange membrane fuel cells, PEMFC, are considered very attractive due to high efficiency and the potential for vehicular and portable applications. However, in order to be competitive economically with other existing power and vehicular systems, the industry needs an efficient methodology for the determination of the optimal project for maximum performance according to desired specifications (e.g., efficiency, power, environmental control), and therefore optimization is one way of lowering costs. The current methodologies are experimentally and computationally expensive for the thermodynamic optimization of complex systems, due to economic restrictions in the effort to develop multiple modifications in the subsystems, without a clearly defined direction, from the physical point of view. An illustrative example is the application of numerical methods to conservation partial differential equations, in diverse phenomena such as in a fuel cell, leading to high cost and computational time even for the simulation of a few selected cases, what practically discards the possibility of an optimization study.

---

[*] Corresponding author. Tel.: +55-41-361-3307; fax: +55-41-361-3129.

E-mail addresses: jvargas@demec.ufpr.br (J.V.C. Vargas), ordonez@eng.fsu.edu (J.C. Ordonez), dalford@duke.edu (A. Bejan).

0017-9310/$ - see front matter © 2004 Elsevier Ltd. All rights reserved.
doi:10.1016/j.ijheatmasstransfer.2004.05.004

Nomenclature

A	area, m^2
A_c	total gas channel cross-sectional area, m^2
A_s	unit fuel cell cross-sectional area, m^2
$\tilde{A}$	dimensionless area
B	dimensionless constant
c_p	specific heat at constant pressure, $kJ\,kg^{-1}\,K^{-1}$
C	constant, Eq. (33)
CV	control volume
D	Knudsen diffusion coefficient, $m^2\,s^{-1}$
E	dimensionless conversion factor, Eqs. (44)–(46)
D_h	gas channel hydraulic diameter, m
f	friction factor
F	Faraday constant, 96,500 $C\,eq^{-1}$
h	heat transfer coefficient, $W\,m^{-2}\,K^{-1}$
$\tilde{h}$	dimensionless heat transfer coefficient
$H_i(T_i)$	molar enthalpy of formation at a temperature T_i of reactants and products, $kJ\,kmol^{-1}$ of compound i
$\widetilde{H}_i(\theta_i)$	dimensionless molar enthalpy of formation at a dimensionless temperature θ_i of reactants and products
H_2 PEMFC	polymer electrolyte membrane fuel cell
$i_{o,a}$, $i_{o,c}$	exchange current densities, $A\,m^{-2}$
$i_{Lim,a}$, $i_{Lim,c}$	limiting current densities, $A\,m^{-2}$
I	current, A
$\tilde{I}$	dimensionless current
j	mass flux, $kg\,s^{-1}\,m^{-2}$
k	thermal conductivity, $W\,m^{-1}\,K^{-1}$
K	permeability, m^2
$\tilde{k}$	dimensionless thermal conductivity
L	control volume length, m
L_c, L_t	gas channels internal dimensions as shown in Fig. 1, m
L_x, L_y, L_z	fuel cell length, width and height, respectively, m
m	mass, kg
$\dot{m}$	mass flow rate, $kg\,s^{-1}$
M	molecular weight, $kg\,kmol^{-1}$
n	equivalent electron per mole of reactant, $eq\,mol^{-1}$
$\dot{n}$	molar flow rate, $kmol\,s^{-1}$
n_c	number of parallel ducts in gas channel
N	dimensionless global wall heat transfer coefficient
p	pressure, $N\,m^{-2}$
$\tilde{p}_s$	perimeter of cross-section, m
P	dimensionless pressure
Pr	Prandtl number, $\mu c_p/k$
q	tortuosity
Q	reaction quotient

$\dot{Q}$	heat transfer rate, W
$\widetilde{Q}$	dimensionless heat transfer rate
r	pore radius, m
R	ideal gas constant, $kJ\,kg^{-1}\,K^{-1}$
$\overline{R}$	universal gas constant, 8.314 $kJ\,kmol^{-1}\,K^{-1}$
Re_{D_h}	Reynolds number based on D_h, $uD_h\rho/\mu$
S	dimensionless conversion factor, Eq. (42)
T	temperature, K
u	mean velocity, $m\ s^{-1}$
$\tilde{u}$	dimensionless mean velocity
U	global wall heat transfer coefficient, $W\,m^{-2}\,K^{-1}$
V	electrical potential, V
V	volume, m^3
V_T	total volume, m^3
$\widetilde{V}$	dimensionless electrical potential
$\widetilde{V}_T$	dimensionless total volume
W	electrical work, J
$\widetilde{W}$	dimensionless fuel cell total electrical power, Eq. (40)
$\widetilde{W}_{net}$	dimensionless fuel cell net power, Eq. (39)
$\widetilde{W}_p$	dimensionless required pumping power, Eq. (41)
x	axial direction, Fig. 1
$y_{2,4,6}$	size constraints
$[\cdot]$	molar concentration of a substance, $mol\,l^{-1}$

Greek symbols

α_a, α_c	anode and cathode charge transfer coefficients
β	electrical resistance, Ω
δ	gas channel aspect ratio
ΔG	molar Gibbs free energy change, $kJ\,kmol^{-1}$ H_2, Eq. (13)
$\Delta\widetilde{G}$	dimensionless Gibbs free energy change
ΔH	molar enthalpy change, $kJ\,kmol^{-1}$ H_2
$\Delta\widetilde{H}$	dimensionless enthalpy change
ΔS	molar entropy change, $kJ\,kmol^{-1}\,K^{-1}$
ζ	stoichiometric ratio
η_a, η_c	anode and cathode charge transfer overpotentials, V
$\eta_{d,a}$, $\eta_{d,c}$	anode and cathode mass diffusion overpotentials, V
η_i	ideal efficiency, Eq. (43)
η_I	first law efficiency, Eq. (44)
η_{II}	second law efficiency, Eq. (45)
η_{net}	net efficiency, Eq. (46)
$\tilde{\eta}_a$, $\tilde{\eta}_c$	dimensionless anode and cathode charge transfer overpotentials
$\tilde{\eta}_{d,a}$, $\tilde{\eta}_{d,c}$	dimensionless anode and cathode mass diffusion overpotentials

$\tilde{\eta}_{ohm}$	dimensionless fuel cell total ohmic potential loss, Eq. (24)
θ	dimensionless temperature
λ	ionomer water content
μ	viscosity, Pa s
ν_i	reaction coefficients
ξ	dimensionless length
ρ	density, kg m^{-3}
σ	electrical conductivity, Ω^{-1} m^{-1}
ϕ	porosity
ψ	dimensionless mass flow rate

Subscripts

a	anode
(aq)	aqueous solution
c	cathode
e	reversible
f	fuel
(g)	gaseous phase
H^+	hydrogen cation
H_2	hydrogen
H_2O	water
i	irreversible
i,a	irreversible at the anode
i,c	irreversible at the cathode
in	control volume inlet
(l)	liquid phase
m	maximum with respect to fuel cell internal structure
mm	maximum with respect to fuel cell internal and external structure
ohm	ohmic
opt	optimal value
out	control volume outlet
ox	oxidant
O_2	oxygen
p	polymer electrolyte membrane
ref	reference level
s,a	anode solid side
s,c	cathode solid side
w	wall
wet	wetted surface
0	initial condition
1, ..., 7	control volumes, Fig. 1
12	interaction between CV1 and CV2
23	interaction between CV2 and CV3
34	interaction between CV3 and CV4
45	interaction between CV4 and CV5
56	interaction between CV5 and CV6
67	interaction between CV6 and CV7
∞	ambient

Superscript

$\circ$	standard conditions [gases at 1 atm, 25 °C, species in solution at 1 M, where M is the molarity = (moles solute)/(liters solution)]

In sum, the current available methodologies seek to find an optimal condition from a group of candidates arbitrarily selected. Therefore, this study is motivated by the need to develop a methodology that provides a structured process to synthesize fuel cell optimal thermodynamic configurations directly from the physical laws. The proposed technique seeks the general direction of flow geometry optimization subject to global constraints (e.g., volume), with the objective of maximizing the net power or the net power density. This approach is general because it may be used in conjunction with other methods of improvement that have been demonstrated, or will be demonstrated, e.g., new materials, and new techniques for separating hydrogen from natural gas inside the fuel cell (internal reforming).

The optimization of flow-system architecture is a widespread occurrence in engineering and nature. Many examples have been brought together under the title of constructal theory [5], which is the thought that geometry (flow architecture) is generated by the pursuit of global performance subject to global constraints, in flow systems the geometry of which is free to change. According to constructal theory, the optimization of flow architecture starts at the smallest (elemental) scale, i.e., in this study, the PEM unit fuel cell. Irreversibilities due to pressure drop, charge transfer and mass diffusion are minimized together. In principle, this procedure can be extended on a hierarchical ladder to larger and more complex systems, to explore multi-scale packings that use the available volume to the maximum. Earlier constructal designs suggest that this approach will lead to high-density constructions with new scaling laws that are dictated by dendritic (space-filling, fractal-like) flow structures. Such designs promise to be robust.

In this paper the optimization is based on a relatively simple model that is sufficiently representative of a fuel cell, i.e., such that the physical trade-offs are clearly present. The technical literature shows several previous PEM fuel cell analytical and numerical models [6–11] either with one- or two-dimensional geometry, isothermal and steady state operation. Zhou and Liu [12] presented a three-dimensional steady state model for proton exchange membrane fuel cells. Among these, two-and three-dimensional models are not suitable for the optimization of flow geometry, because they would require the solving of partial differential equations for flow simulation in a very large number of flow configurations. No model was found in the literature that addresses the spatial temperature and pressure gradients in a unit PEM fuel cell, pressure drops in the gas channels and their effect on performance.

The geometric optimization alternative chosen in this paper was introduced in a previous study for an alkaline fuel cell, which divides the fuel cell into several control volumes that correspond to the most representative parts of the flow system [13]. All the flow phenomena that are present are taken into account. The result is a model with unidirectional internal flow that contains additional three-dimensional features such as the electrode wetted area; heat transfer between the cell, fuel, oxidant and the surroundings, and pressure drops in the gas channels. The model is represented by a system of algebraic equations, the solution of which consists of the temperatures and pressures of each control volume, and the polarization and net power curves for the whole system. The model is simple enough to insure small computational time requirements, so that it is possible to simulate the flow in a very large number of competing flow configurations.

2. Mathematical model

The main features of a hydrogen polymer electrolyte membrane fuel cell (H_2 PEMFC) are shown in Fig. 1.

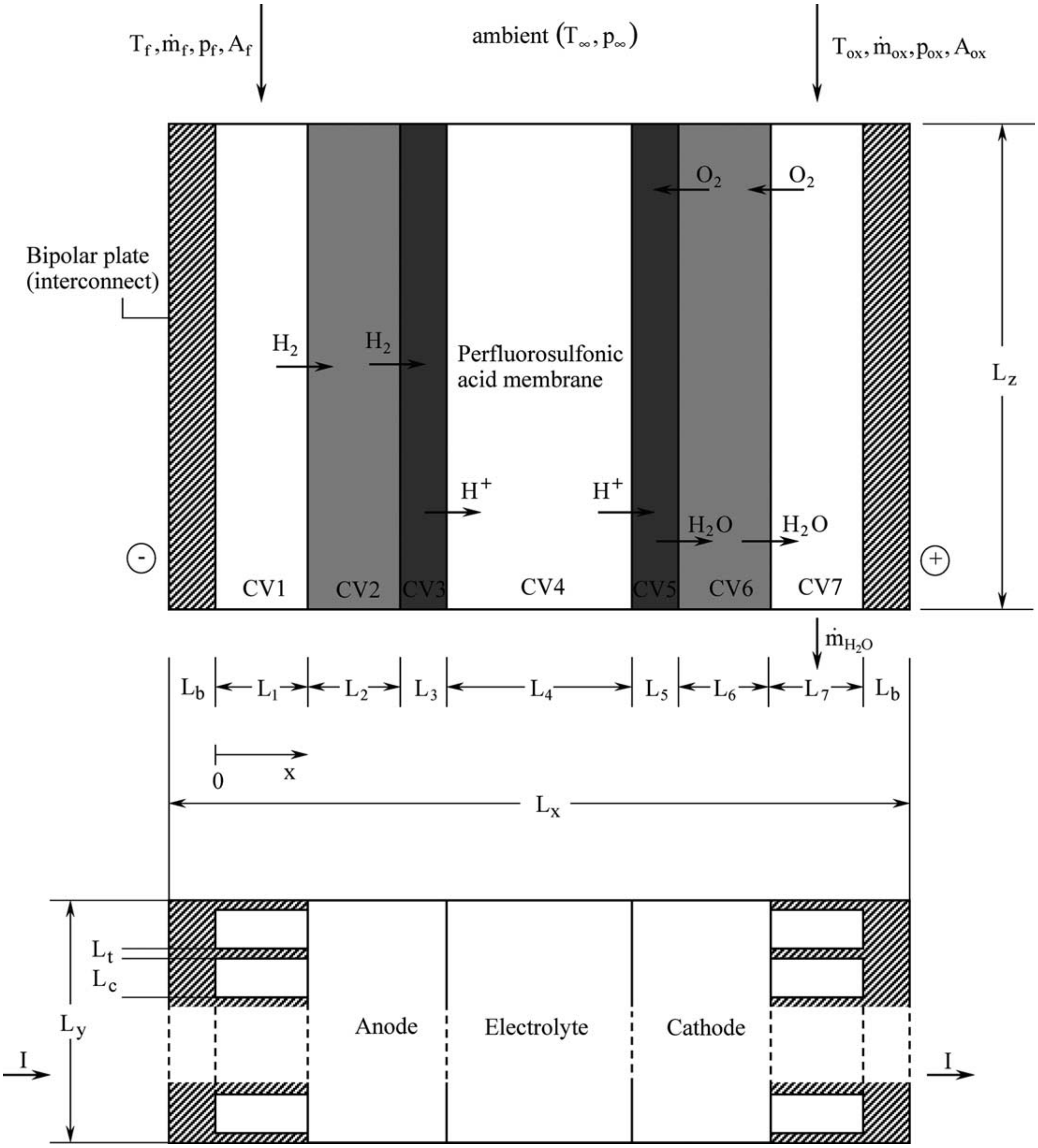

Fig. 1. Model of the PEM unit fuel cell.

The fuel may be pure hydrogen, or a diluted hydrogen mixture generated from a hydrocarbon reformation process. For simplicity, the model is based on the assumption that the fuel stream is pure hydrogen, and that the oxidant is pure oxygen.

The fuel cell is divided into seven control volumes that interact energetically with one another. The fuel cell also interacts with adjacent fuel cells in a package, and/or with the ambient. Additionally, two bipolar plates (interconnects) are presented: these have the function of allowing the electrons produced by the electrochemical oxidation reaction at the anode to flow to the external circuit or to an adjacent cell. The control volumes (CV) are the fuel channel (CV1), the anode diffusion-backing layer (CV2), the anode reaction layer (CV3), the polymer electrolyte membrane (CV4), the cathode reaction layer (CV5), the cathode diffusion backing layer (CV6) and the oxidant channel (CV7).

The model consists of the conservation equations for each control volume, and the equations accounting for electrochemical reactions, where reactions are present. The reversible electrical potential and power of the fuel cell are then computed (based on the reactions) as functions of the temperature and pressure fields determined by the model. The actual electrical potential and power of the fuel cell are obtained by subtracting from the reversible potential the losses due to surface overpotentials (poor electrocatalysis), slow diffusion and all internal ohmic losses through the cell (resistance of individual cell components, including electrolyte membrane, bipolar plates, interconnects and any other cell components through which electrons flow). These are functions of the total cell current (I), which is directly related to the external load (or the cell voltage). In sum, the total cell current is considered an independent variable in this study. The following analysis is for steady-state fuel cell operation.

Dimensionless variables are defined based on the geometric and operating parameters of the system. Pressures and temperatures are referenced to ambient conditions: $P_i = p_i/p_\infty$ and $\theta_i = T_i/T_\infty$. The dimensionless mass flow rates are defined as

$$\psi = \frac{\dot{m}_i}{\dot{m}_{\mathrm{ref}}}, \tag{1}$$

where the subscript i represents a substance that flows through the fuel cell, and $\dot{m}_{\mathrm{ref}}$ is a specified reference mass flow rate. Additional dimensionless variables are

$$N_i = \frac{U_{\mathrm{w}i} V_{\mathrm{T}}^{2/3}}{\dot{m}_{\mathrm{ref}} c_{p,\mathrm{f}}}, \quad \tilde{A}_i = \frac{A_i}{V_{\mathrm{T}}^{2/3}}, \tag{2}$$

where subscript i indicates a substance or a location in the fuel cell; N is the dimensionless global wall heat transfer coefficient, and $\tilde{A}$ is the dimensionless area. In Eqs. (1) and (2), p_∞ is the ambient pressure, T_∞ is the ambient temperature, and $c_{p,i}$ is the specific heat at constant pressure.

The total volume of the fuel cell, $V_{\mathrm{T}} = L_x L_y L_z$, is finite and fixed. This is a realistic design constraint, which accounts for the finiteness of the available space and the general push for doing the most with limited resources (e.g., space). The maximization of performance for the specified volume means the maximization of performance *density*. The fixed length scale $V_{\mathrm{T}}^{1/3}$ is used for the purpose of non-dimensionalizing all the lengths that characterize the fuel cell geometry,

$$\xi_j = \frac{L_j}{V_{\mathrm{T}}^{1/3}}, \tag{3}$$

where the subscript j indicates a particular dimension of the fuel cell geometry, Fig. 1.

The wall heat transfer area of one control volume is $A_{\mathrm{w}i} = \tilde{p}_{\mathrm{s}} L_i$ $(2 \leqslant i \leqslant 6)$ and $A_{\mathrm{w}i} \cong \tilde{p}_{\mathrm{s}} L_i + L_y L_z$ $(i = 1, 7$; assuming that $L_{\mathrm{t}} \ll L_{\mathrm{c}}$ in Fig. 1), where $\tilde{p}_{\mathrm{s}} = 2(L_y + L_z)$ is the perimeter of the fuel cell cross-section. The control volumes are $V_j = L_y L_z L_j$ $(2 \leqslant j \leqslant 6)$ and $V_j = n_{\mathrm{c}} L_{\mathrm{c}} L_l L_z$ $(j = 1, 7)$, where n_{c} is the integer part of $L_y/(L_{\mathrm{t}} + L_{\mathrm{c}})$, i.e., the number of parallel ducts in each gas channel (fuel and oxidant).

The fuel pressure (p_{f} in CV1) and oxidant pressure (p_{ox} in CV7) are assumed known and constant during fuel cell operation. The stoichiometric ratio for an electrode reaction is defined as the provided reactant (mol s^{-1}) divided by the reactant needed for the electrochemical reaction of interest. In the present model, stoichiometric ratios greater than 1 are prescribed on the fuel side (ζ_1) and oxidant side (ζ_7). The mass and energy balances for CV1 yield the temperature in CV1,

$$\widetilde{Q}_{\mathrm{w}1} + \psi_{\mathrm{f}}(\theta_{\mathrm{f}} - \theta_1) + \widetilde{Q}_{12} + \widetilde{Q}_{1\mathrm{ohm}} = 0 \tag{4}$$

where $\widetilde{Q}_{\mathrm{w}i} = N_i \tilde{A}_{\mathrm{w}i}(1 - \theta_i)$, where subscript i refers to one of the control volumes, $\widetilde{Q}_{12} = \tilde{h}_1 \tilde{A}_{\mathrm{s}}(1 - \phi_2)(\theta_2 - \theta_1)$, $\tilde{h}_1 = h_1 V_{\mathrm{T}}^{2/3}/(\dot{m}_{\mathrm{ref}} c_{p,\mathrm{f}})$, ϕ_i are the porosities, and $\tilde{A}_{\mathrm{s}} = L_y L_z / V_{\mathrm{T}}^{2/3}$ is the dimensionless cross-sectional area of the fuel cell. The dimensionless heat transfer rates for all the compartments are $\widetilde{Q}_i = \dot{Q}_i/(\dot{m}_{\mathrm{ref}} c_{p,\mathrm{f}} T_\infty)$, where i accounts for any of the heat transfer interactions that are present in the model. The ohmic heating is $\widetilde{Q}_{i\mathrm{ohm}} = I^2 \beta_i/(\dot{m}_{\mathrm{ref}} c_{p,\mathrm{f}} T_\infty)$, where subscript i refers to a control volume (1–7), and β (Ω) is the electrical resistance.

Next is the anode backing diffusion layer (CV2), where reactions are absent. Both electrodes in a fuel cell are porous, such that a large real wetted surface area can be obtained to provide good contact between the electrode and the electrolyte (ionomer) and, therefore, large power densities. Although the porous medium consists of a solid side and a fluid side, the mass of fluid in CV2 is negligible relative to the mass of solid, therefore only the solid is taken into account in the energy balance. The net heat transfer rates are $\widetilde{Q}_2 = -\widetilde{Q}_{12} + \widetilde{Q}_{\mathrm{w}2} + \widetilde{Q}_{23} + \widetilde{Q}_{2\mathrm{ohm}}$, where $\widetilde{Q}_{23} = -\tilde{k}_{s,a}(1-\phi_2)\tilde{A}_s(\theta_2-\theta_3)/[(\xi_2+\xi_3)/2]$. The dimensionless thermal conductivity is defined by $\tilde{k}_i = k_i V_T^{1/3}/(\dot{m}_{ref} c_{p,f})$.

The wetted areas in the porous anode and cathode are estimated by assuming dual-porosity electrodes, as shown in Fig. 2. The pores are approximated as parallel tubes with an average diameter of the same order as the square root of the porous medium permeability, $K^{1/2}$. Therefore, the wetted area for each porous control volume is $A_{j,\mathrm{wet}} = 4\phi_j L_j K_j^{-1/2} A_s$, where K_j are the permeabilities.

The hydrogen mass flow rate required for the current (I) dictated by the external load is

$$\dot{m}_{H_2} = \dot{n}_{H_2} M_{H_2} = \frac{I}{nF} M_{H_2}, \tag{5}$$

where $\dot{n}_i$ is the molar flow rate for species i, M_i the molecular weight of species i, n the number of moles of electrons formed in the reaction and F the Faraday constant, 96,500 C eq^{-1}.

Therefore, the oxygen mass flow rate needed for a PEM fuel cell is

$$\dot{m}_{O_2} = \tfrac{1}{2}\dot{n}_{H_2} M_{O_2}. \tag{6}$$

Diffusion is assumed to be the dominant transport mechanism across the diffusion and catalyst layers. For Knudsen flow, the fuel and oxidant mass fluxes in the porous layers are given by [14]

$$j_i = -[D(\rho_{\mathrm{out}} - \rho_{\mathrm{in}})/L]_i, \quad i = 2, 6, \tag{7}$$

where $D = B\{r[8\overline{R}T/(\pi M)]^{1/2}\phi^q\}$ is the Knudsen diffusion coefficient, ρ the density, $\overline{R}$ the universal gas constant, ϕ the porosity, q the tortuosity [15,16], and B is a correction coefficient. By using Eq. (7) and the ideal gas model for H_2 and O_2, we find the pressures of the hydrogen and oxygen that enter the catalyst layers

$$P_{i,\mathrm{out}} = P_{i,\mathrm{in}} - \frac{j_i R_i T_\infty L_i \theta_i}{D_i p_\infty}, \quad i = 2, 6, \tag{8}$$

where $j_2 = \dot{m}_{H_2}/A_{3,\mathrm{wet}}$ and $j_6 = \dot{m}_{O_2}/A_{5,\mathrm{wet}}$, and $A_{3,\mathrm{wet}}$ and $A_{5,\mathrm{wet}}$ are the wetted areas in the porous catalyst layers. Note also that $P_{2,\mathrm{in}} = P_f$ and $P_{6,\mathrm{in}} = P_{\mathrm{ox}}$. The average pressures in CV2 and CV6 are estimated as

$$P_i = \tfrac{1}{2}(P_{i,\mathrm{in}} + P_{i,\mathrm{out}}), \quad i = 2, 6. \tag{9}$$

The energy balance delivers the CV2 temperature,

$$\theta_1 - \theta_2 + \frac{\widetilde{Q}_2}{\psi_{H_2}} = 0. \tag{10}$$

In the anode reaction layer (CV3), the electrical current is generated by the electrochemical oxidation reaction,

$$H_{2(g)} \rightarrow 2H^+_{(aq)} + 2e^- \tag{11}$$

where a perfluorosulfonic acid membrane (e.g., Nafion 117 by DuPont) has been assumed in the electrolyte.

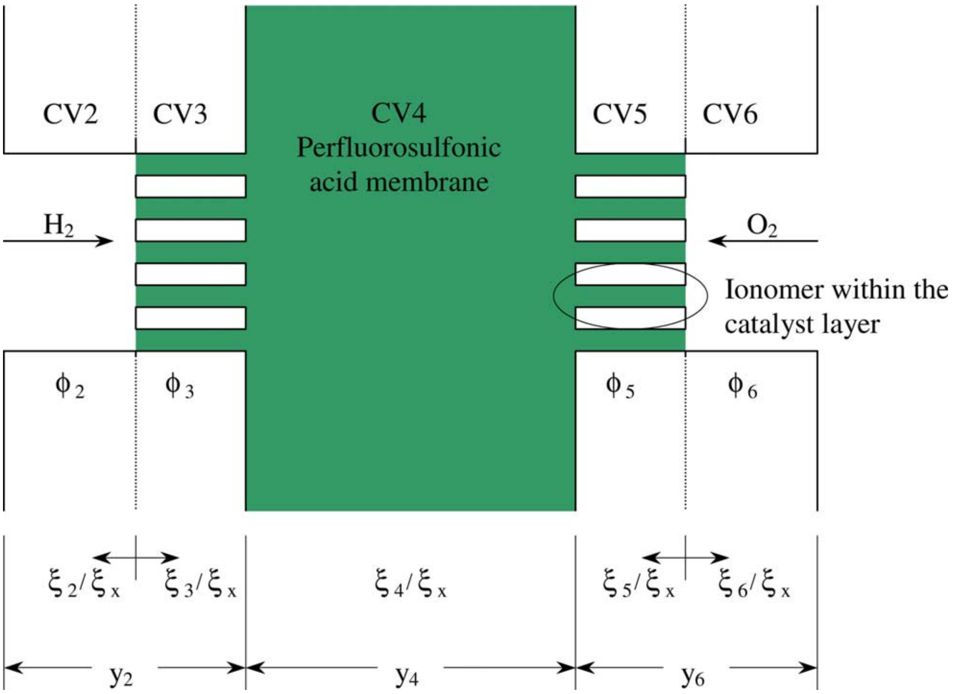

Fig. 2. Cross-sectional detail of dual porosity electrodes and the internal structure optimization procedure.

CV3 is divided into two compartments, the solid and the liquid solution that form the anode reaction layer. However, in the thermal analysis only the solid is taken into account, because the mass of fluid in CV3 is negligible in comparison with the mass of solid. The dimensionless net heat transfer in CV3 is given by $\widetilde{Q}_3 = -\widetilde{Q}_{23} + \widetilde{Q}_{w3} + \widetilde{Q}_{34} + \widetilde{Q}_{3ohm}$. The heat transfer rate between CV3 and CV4 (the polymer electrolyte membrane) is dominated by conduction, therefore $\widetilde{Q}_{34} = -(1-\phi_3)(\theta_3 - \theta_4)\widetilde{A}_s 2\tilde{k}_{s,a}\tilde{k}_p/(\xi_4\tilde{k}_{s,a} + \xi_3\tilde{k}_p)$.

The mass and energy balances for CV3, together with the anode reaction equation deliver the relations $\dot{n}_{H_2} = \dot{m}_{H_2}/M_{H_2}$, $\dot{n}_{H^+} = 2\dot{n}_{H_2}$, $\dot{m}_{H^+} = 2\dot{n}_{H_2}M_{H^+}$ and

$$\widetilde{Q}_3 - \Delta\widetilde{H}_3 + \Delta\widetilde{G}_3 = 0, \tag{12}$$

where, $(\Delta\widetilde{H}_3, \Delta\widetilde{G}_3) = \dot{n}_{H_2}(\Delta H_3, \Delta G_3)/(\dot{m}_{ref}c_{p,f}T_\infty)$.

The dimensionless enthalpy of formation is defined by $\widetilde{H}_i = \dot{n}_i H_i/(\dot{m}_{ref}c_{p,f}T_\infty)$, where the subscript i refers to a substance or a control volume. The enthalpy change due to the anode reaction is given by $\Delta H_3 = \sum_{products}[v_i H_i(T_i)] - \sum_{reactants}[v_i H_i(T_i)]$ and $W_{e3} = -\Delta G_3$, ΔH_3 is the CV3 reaction enthalpy change (kJ kmol^{-1} H$_2$); v_i are the stoichiometric coefficients; $H_i(T_i)$ is the molar enthalpy (kJ kmol^{-1}) of formation at a temperature T_i of reactants and products of compound i; ΔG_3 is the CV3 reaction Gibbs free energy change (kJ kmol^{-1} H$_2$) and W_{e3} is the maximum (reversible) electrical work generated due to the reaction in CV3 (kJ kmol^{-1} H$_2$).

The molar enthalpies of formation are obtained from tabulated values [17,18] at T_2 for $H_{2(g)}$ and T_3 for $H^+_{(aq)}$, and at 1 atm, because ΔH is independent of pressure. The reaction Gibbs free energy change, ΔG, is a function of temperature, pressure and concentrations,

$$\Delta G = \Delta G^\circ + \overline{R}T\ln Q, \tag{13}$$

where $\Delta G^\circ = \Delta H^\circ - T\Delta S^\circ$ is the standard Gibbs free energy (kJ kmol^{-1} H$_2$); ΔH° is the standard enthalpy change (kJ kmol^{-1}); ΔS° is the standard entropy change (kJ kmol^{-1} K^{-1}) [gases at 1 atm, 25 °C, species in solution at 1 M, where M is the molarity = (moles solute)/(liters solution)]; $\overline{R}$ is the universal ideal gas constant, and Q is the reaction quotient. The reaction quotient Q has the same mathematical form as the reaction equilibrium constant: the difference is that the terms that appear in Q are instantaneous pressures and concentrations rather than equilibrium values. Therefore, in the present reaction [Eq. (11)] the resulting expression for Q_3 is $Q_3 = [H^+_{(aq)}]^2/p_{H_2}$, where $[H^+_{(aq)}]$ is the molar concentration of the acid solution, (mol l^{-1}), and $p_{H_2} = p_{2,out}$, i.e., the partial pressure of H$_2$ in atmospheres at the CV2 outlet. Recall that pure liquids or solids do not appear in the calculation of Q_3; neither does the solvent in a dilute solution.

In a polymer electrolyte membrane, water content (λ) is described as the ratio of the number of water molecules to the number of charge sites, i.e., the number of ions, $SO_3^-H^+$. Zawodzinski et al. [19] measured water content for the Nafion 117 membrane, and found that, for equilibrium with saturated water vapor, $\lambda = 14$ at 30 °C. Springer et al. [6] found that water vapor and liquid water (in equilibrium with each other) equilibrate separately to different membrane water contents, namely, $\lambda = 16.8$ at 80 °C and $\lambda = 22$ at 100 °C. Because the presence of liquid water in contact with the ionomer is discrete rather than continuous, the water concentration in the ionomer (within the catalyst layer) may not be uniform. Because the present model is in essence macro-homogeneous, it is assumed that all ingredients of the catalyst layer are evenly distributed, and that the liquid water product is evenly distributed. Therefore, the water content in ionomer (within the catalyst layer) is assumed constant: this corresponds to the value measured when the ionomer is in contact with liquid water, or to some average between this value and the value corresponding to when the ionomer is in contact with saturated water vapor [8]. Usually, the anode water content in the anode is different than in the cathode; therefore for assumed values of λ_a (anode water content) and λ_c (cathode water content), and by assuming a linear variation of the water content along the membrane thickness, the average water content in the membrane is defined as

$$\lambda = \frac{\lambda_a + \lambda_c}{2}. \tag{14}$$

Eq. (14) allows the calculation of $[H^+_{(aq)}]$ as a function of λ, namely $[H^+_{(aq)}] \cong \rho_{H_2O}/(\lambda M_{H_2O})$ for a dilute water solution. The present model also assumes that the volume fraction of ionomer in the catalyst layer is approximately equal to the porosity either in CV3 or CV5, as shown in Fig. 2.

The reversible electrical potential at the anode is given by the Nernst equation [18],

$$V_{e,a} = V^\circ_{e,a} - \frac{\overline{R}T_3}{nF}\ln Q_3, \tag{15}$$

where $V_{e,a} = \Delta G_3/(-nF)$ and $V^\circ_{e,a} = \Delta G^\circ_3/(-nF)$. At the anode there are two mechanisms for potential losses: (i) charge transfer, and (ii) mass diffusion. The potential loss due to charge transfer is obtained implicitly from the Butler–Volmer equation for a given current I [20,21]

$$\frac{I}{A_{3,wet}} = i_{o,a}\left[\exp\left\{\frac{(1-\alpha_a)\eta_a F}{\overline{R}T_3}\right\} - \exp\left\{-\frac{\alpha_a\eta_a F}{\overline{R}T_3}\right\}\right], \tag{16}$$

where η_a is the potential loss at the anode, α_a is the anode charge transfer coefficient, and $i_{o,a}$ is the anode exchange current density (a function of catalyst type, catalyst layer morphology, temperature and pressure). The potential loss due to mass diffusion is [20]

$$\eta_{d,a} = \frac{\overline{R}T_3}{nF}\ln\left(1 - \frac{I}{A_{3,wet}\, i_{Lim,a}}\right). \tag{17}$$

In Eq. (17) the limiting current density at the anode ($i_{Lim,a}$) occurs at high values of the surface overpotential, when the gas is completely depleted in the very thin active catalyst layer fraction situated at the interface with the gas diffuser, i.e., $P_{2,out} = 0$. Therefore, Eq. (8) is rearranged as

$$i_{Lim,a} = \frac{P_f p_\infty D_2 nF}{M_{H_2} L_2 R_f \theta_2 T_\infty}. \tag{18}$$

The dimensionless potentials are defined based on a reference voltage, V_{ref}, namely $\widetilde{V}_i = V_i/V_{ref}$ and $\widetilde{\eta} = \eta_i/V_{ref}$, where subscript i accounts for all the potentials that are present in the fuel cell. The resulting electrical potential at the anode is $\widetilde{V}_{i,a} = \widetilde{V}_{e,a} - \widetilde{\eta}_a - |\widetilde{\eta}_{d,a}|$, where we have taken the absolute value of $\widetilde{\eta}_{d,a}$, because $\widetilde{\eta}_{d,a} < 0$ (cathodic overpotential).

Next is the analysis of the polymer electrolyte membrane (CV4), which interacts with CV3, CV5 and the ambient. In the cathode reaction layer (CV5), the reaction is

$$\tfrac{1}{2}O_{2(g)} + 2e^- + 2H^+_{(aq)} \rightarrow H_2O_{(l)} \tag{19}$$

Eqs. (11) and (19) and the conservation of mass in CV4 require $2\dot{n}_{H_2} = \dot{n}_{H^+,out} = \dot{n}_{H^+,in} = 2\dot{n}_{O_2}$. In conclusion, $\dot{n}_{O_2} = \dot{n}_{H_2}$, where $\dot{n}_{O_2} = 2\dot{m}_{O_2}/M_{O_2}$. Accordingly, the required oxidant mass flow rate is $\dot{m}_{O_2} = \dot{m}_{H_2}M_{O_2}/(2M_{H_2})$. The net heat transfer in CV4 is obtained from $\widetilde{Q}_4 = -\widetilde{Q}_{34} + \widetilde{Q}_{w4} + \widetilde{Q}_{45} + \widetilde{Q}_{4ohm}$ and $\widetilde{Q}_{45} = -(1-\phi_5)(\theta_4 - \theta_5)\widetilde{A}_s 2\widetilde{k}_{s,c}\widetilde{k}_p/(\xi_4\widetilde{k}_{s,c} + \xi_5\widetilde{k}_p)$. Next, the CV4 temperature is obtained from

$$\widetilde{Q}_4 + \widetilde{H}(\theta_3)_{H^+_{(aq)}} - \widetilde{H}(\theta_4)_{H^+_{(aq)}} = 0. \tag{20}$$

The internal ohmic losses are usually dominated by the low electrolyte conductivity. However, to allow us to study the effect of varying the thickness of the reacting layers, the model also accounts for the potential loss due to the electrical resistance posed by the ionomer within the porous reaction layers present in CV3 and CV5. The ionic conductivity, σ ($\Omega^{-1}\,m^{-1}$), of Nafion 117 as a function of temperature is given by the following empirical formula [6]:

$$\sigma_i(\theta) = \exp\left[1268\left(\frac{1}{303} - \frac{1}{\theta_i T_\infty}\right)\right](0.5139\lambda_i - 0.326), \quad i = 3,4,5. \tag{21}$$

Based on the electrical conductivities and geometry of each compartment, the electrical resistances, β (Ω), are given by

$$\beta_i = \frac{\xi_i}{\widetilde{A}_s V_T^{1/3}\sigma_i(1-\phi_i)}, \quad i = 1,2,6,7, \tag{22}$$

$$\beta_i = \frac{\xi_i}{\widetilde{A}_s V_T^{1/3}\sigma_i\phi_i}, \quad i = 3,4,5 \ (\phi_4 = 1). \tag{23}$$

Therefore, the total dimensionless ohmic loss in the space from CV1 to CV7 is

$$\widetilde{\eta}_{ohm} = \frac{I}{V_{ref}}\sum_{i=1}^{7}\beta_i. \tag{24}$$

The conductivities of the catalyst layers are given by $\sigma_3\phi_3$ and $\sigma_5\phi_5$, according to Eqs. (21) and (23), which agrees qualitatively with previously measured catalyst layers ionic conductivities [22], i.e., the ionic conductivity increases with increasing Nafion content, which increases as ϕ increases in the present model. Additionally, as a quantitative example of the use of Eqs. (21) and (23), the product $\sigma\phi$ leads to a resistivity of 40.29 Ωcm, for $\lambda = 14$, $\phi = 0.2$ and $T = 80$ °C, which agrees with a previously reported catalyst layer electronic resistivity of 40 Ωcm [23]. The conductivities of the diffusive layers, σ_2 and σ_6, are the carbon-phase conductivities [9]. Finally, the conductivities of CV1 and CV7, σ_1 and σ_7, are the electrical conductivities of the bipolar plates material. Eq. (22) accounts for the void fractions of CV1 and CV7, i.e., $\phi_1 = \phi_7 = \xi_c/(\xi_t + \xi_c)$, computed for any particular fuel cell internal geometry according to Fig. 1.

The analysis in the cathode reaction layer (CV5) is analogous to what we presented for the anode reaction layer (CV3). This time the reaction equation is Eq. (19). CV5 is also divided into two compartments, fluid and solid, but in the thermal analysis, only the solid is taken into account. The dimensionless net heat transfer in CV5 is given by $\widetilde{Q}_5 = -\widetilde{Q}_{45} + \widetilde{Q}_{w5} + \widetilde{Q}_{56} + \widetilde{Q}_{5ohm}$, with $\widetilde{Q}_{56} = -\widetilde{k}_{s,c}(1-\phi_6)\widetilde{A}_s(\theta_5 - \theta_6)/[(\xi_5 + \xi_6)/2]$.

The mass and energy balances in CV5, in conjunction with Eq. (20) deliver $\dot{n}_{H^+,in} = 2\dot{n}_{O_2}, \dot{n}_{H_2O,out} = \dot{n}_{O_2}$, and

$$\widetilde{Q}_5 - \Delta\widetilde{H}_5 + \Delta\widetilde{G}_5 = 0 \tag{25}$$

where $(\Delta\widetilde{H}_5, \Delta\widetilde{G}_5) = \dot{n}_{O_2}(\Delta H_5, \Delta G_5)/(\dot{m}_{ref}c_{p,f}T_\infty)$. The enthalpy change during cathode reaction is $\Delta H_5 = \sum_{products}[\nu_i H_i(T_i)] - \sum_{reactants}[\nu_i H_i(T_i)]$, while $W_{e5} = -\Delta G_5$ is the change in Gibbs free energy and W_{e5} is the maximum (reversible) electrical work generated by the reaction in CV5. The molar enthalpies of formation, $H_i(T_i)$, are obtained from tabulated values [17,18] at T_6 for $O_{2(g)}$, T_4 for $H^+_{(aq)}$ and T_5 for $H_2O_{(l)}$ at 1 atm. The change in the Gibbs free energy ΔG_5 for the reaction of Eq. (19) is calculated by using Eq. (13). The CV5 reaction quotient is therefore $Q_5 = \{[H^+_{(aq)}]^2 p_{O_2}^{1/2}\}^{-1}$, where $p_{O_2} = p_{6,out}$. The reversible electrical potential at the cathode results from Eq. (15) after using $V_{e,c}$, $V^\circ_{e,c}$, ΔG_5, ΔG°_5, T_5 and Q_5 in place of $V_{e,a}$, $V^\circ_{e,a}$, $\Delta G_3\Delta G^\circ_3$, T_3 and Q_3.

The analysis for the cathode reaction layer (CV5) follows the same path as for the anode reaction layer (CV3). The potential losses are due to charge transfer and mass diffusion. The potential loss due to charge transfer is obtained through Eq. (16), using $A_{5,\mathrm{wet}}$, $i_{\mathrm{o,c}}$, α_{c}, η_{c} and T_5, in place of $A_{3,\mathrm{wet}}$, $i_{\mathrm{o,a}}$, α_{a}, η_{a} and T_3, respectively. The potential loss due to mass diffusion is calculated based on Eq. (17) by using $\eta_{\mathrm{d,c}}$, T_5, $A_{5,\mathrm{wet}}$ and $i_{\mathrm{Lim,c}}$, in place of $\eta_{\mathrm{d,a}}$, T_3, $A_{3,\mathrm{wet}}$ and $i_{\mathrm{Lim,a}}$, respectively.

The limiting current density at the cathode ($i_{\mathrm{Lim,c}}$), is calculated using the same reasoning as for CV3, based on Eq. (8), such that

$$i_{\mathrm{Lim,c}} = \frac{2P_{\mathrm{ox}} p_\infty D_6 nF}{M_{\mathrm{O_2}} L_6 R_{\mathrm{ox}} \theta_6 T_\infty}. \tag{26}$$

Finally, the dimensionless electrical potential at the cathode is $\widetilde{V}_{i,\mathrm{c}} = \widetilde{V}_{\mathrm{e,c}} - \tilde{\eta}_{\mathrm{c}} - |\tilde{\eta}_{\mathrm{d,c}}|$.

The mass balance for CV6 yields $\dot{m}_{\mathrm{O_2,out}} = \dot{m}_{\mathrm{O_2,in}} = \dot{m}_{\mathrm{O_2}}$ and $\dot{n}_{\mathrm{H_2O}} = \dot{n}_{\mathrm{H_2O,out}} = \dot{n}_{\mathrm{H_2O,in}} = \dot{n}_{\mathrm{O_2}}$. The dimensionless net heat transfer rate in CV6 results from $\widetilde{Q}_6 = -\widetilde{Q}_{56} + \dot{Q}_{\mathrm{w6}} + \widetilde{Q}_{67} + \widetilde{Q}_{6\mathrm{ohm}}$, with $\widetilde{Q}_{67} = \tilde{h}_7 \tilde{A}_{\mathrm{s}} (1 - \phi_6)(\theta_7 - \theta_6)$, $\tilde{h}_7 = h_7 V_{\mathrm{T}}^{2/3} / (\dot{m}_{\mathrm{ref}} c_{p,\mathrm{f}})$. The dimensionless temperature for CV6 is given by

$$\widetilde{Q}_6 + \psi_{\mathrm{O_2}} \frac{c_{p,\mathrm{ox}}}{c_{p,\mathrm{f}}} (\theta_7 - \theta_6) + \widetilde{H}(\theta_5)_{\mathrm{H_2O}} - \widetilde{H}(\theta_6)_{\mathrm{H_2O}} = 0. \tag{27}$$

The dimensionless net heat transfer rate in CV7 is $\widetilde{Q}_7 = -\widetilde{Q}_{67} + \widetilde{Q}_{\mathrm{w7}} + \widetilde{Q}_{7\mathrm{ohm}}$. The balances for mass and energy in the oxidant channel (CV7), the assumptions of non-mixing flow, and the assumption that the space is filled mainly with dry oxygen, yield $\dot{m}_{\mathrm{H_2O}} = \dot{m}_{\mathrm{H_2O,in}} = \dot{m}_{\mathrm{H_2O,out}} = \dot{n}_{\mathrm{O_2}} M_{\mathrm{H_2O}}$ and

$$\widetilde{Q}_7 + \psi_{\mathrm{ox}} \frac{c_{p,\mathrm{ox}}}{c_{p,\mathrm{f}}} (\theta_{\mathrm{ox}} - \theta_7) + \widetilde{H}(\theta_6)_{\mathrm{H_2O}} - \widetilde{H}(\theta_7)_{\mathrm{H_2O}} = 0. \tag{28}$$

3. Shape optimization

The model constructed in Section 2 allows us to calculate the response of the fuel cell when its geometry and operating parameters change. The model accounts for temperature and pressure gradients and potential losses. An important step in thermodynamic optimization is the identification of realistic design constraints. The volume constraint is

$$\xi_x \xi_y \xi_z = 1. \tag{29}$$

Additional constraints are the stoichiometric ratios in the fuel and oxidant channels, ζ_1 and ζ_7. Therefore the inlet mass flow rates are $\psi_{\mathrm{f}} = \zeta_1 \psi_{\mathrm{H_2}}$ and $\psi_{\mathrm{ox}} = \zeta_7 \psi_{\mathrm{O_2}}$, where $\psi_{\mathrm{H_2}}$ and $\psi_{\mathrm{O_2}}$ are obtained through Eqs. (5) and (6).

Assuming that the channels are straight and sufficiently slender, and using the ideal gas model, we can express the pressure drops as

$$\Delta P_i = n_{\mathrm{c}} f_i \left(\frac{\xi_z}{\xi_i} + \frac{\xi_z}{\xi_{\mathrm{c}}} \right) \frac{P_j}{\theta_i} \frac{R_{\mathrm{f}}}{R_i} \tilde{u}_i^2, \tag{30}$$

where $i = 1, 7$ and $j = \mathrm{f}, \mathrm{ox}$, respectively. Here $\tilde{u}_i = (\tilde{u}_{i,\mathrm{in}} + \tilde{u}_{i,\mathrm{out}})/2$ is the channel dimensionless mean velocity, defined as $\tilde{u} = u/(R_{\mathrm{f}} T_\infty)^{1/2}$, and f is the friction factor. According to mass conservation, the dimensionless mean velocities in the gas channels are

$$\tilde{u}_1 = \frac{C\theta_1}{\tilde{A}_{\mathrm{c}1} P_{\mathrm{f}}} \left[\psi_{\mathrm{f}} - \frac{\psi_{\mathrm{H_2}}}{2} \right], \tag{31}$$

$$\tilde{u}_7 = \frac{R_{\mathrm{ox}} C \theta_7}{R_{\mathrm{f}} \tilde{A}_{\mathrm{c}7} P_{\mathrm{ox}}} \left[\psi_{\mathrm{ox}} - \frac{\psi_{\mathrm{O_2}}}{2} \right], \tag{32}$$

$$C = \frac{(R_{\mathrm{f}} T_\infty)^{1/2} \dot{m}_{\mathrm{ref}}}{p_\infty V_{\mathrm{T}}^{2/3}}, \tag{33}$$

where $\tilde{A}_{\mathrm{c}i} = n_{\mathrm{c}} L_{\mathrm{c}} L_i / V_{\mathrm{T}}^{2/3}$, $i = 1, 7$, is the dimensionless total duct cross section area in the fuel and oxidant channels, respectively. Eqs. (30)–(33) deliver the pressure drops, ΔP_1 and ΔP_7, and mean velocities for both fuel and oxidant gas channels for each tested geometry during the shape optimization process.

The model also requires the evaluation of the friction factor and heat transfer coefficients in the gas channels. For the laminar regime ($Re_{D_{\mathrm{h}}} < 2300$) we used the correlations [24]

$$f_i Re_{D_{\mathrm{h},i}} = 24(1 - 1.3553\delta_i + 1.9467\delta_i^2 - 1.7012\delta_i^3 + 0.9564\delta_i^4 - 0.2537\delta_i^5), \tag{34}$$

$$\frac{h_i D_{\mathrm{h},i}}{k_i} = 7.541(1 - 2.610\delta_i + 4.970\delta_i^2 - 5.119\delta_i^3 + 2.702\delta_i^4 - 0.548\delta_i^5), \tag{35}$$

where $\delta_i = L_{\mathrm{c}}/L_i$, for $L_{\mathrm{c}} \leqslant L_i$ and $\delta_i = L_i/L_{\mathrm{c}}$, for $L_{\mathrm{c}} > L_i$; $D_{\mathrm{h},i} = 2L_{\mathrm{c}} L_i/(L_{\mathrm{c}} + L_i)$, $Re_{D_{\mathrm{h},i}} = u_i D_{\mathrm{h},i} \rho_i / \mu_i$ and $i = 1, 7$. The correlations used for the turbulent regime were [25]

$$f_i = 0.079 Re_{D_{\mathrm{h}}}^{-1/4} \quad (2300 < Re_{D_{\mathrm{h},i}} < 2 \times 10^4), \tag{36}$$

$$\frac{h_i D_{\mathrm{h},i}}{k_i} = \frac{(f_i/2)(Re_{D_{\mathrm{h},i}} - 10^3) Pr_i}{1 + 12.7 (f_i/2)^{1/2} (Pr^{2/3} - 1)} \quad (2300 < Re_{D_{\mathrm{h},i}} < 5 \times 10^6), \tag{37}$$

where Pr is the gas Prandtl number, $\mu c_p/k$.

According to Fig. 1, the architecture of the fuel cell is determined completely by the internal structure ($L_x = 2L_{\mathrm{b}} + \sum_{i=1}^{7} L_i$) and the external shape (L_x, L_y, L_z) for a constrained volume, V_{T}. The optimization objective is to determine the system architecture: the optimal allocation of volume, such that the total net power is maximized. The appropriate figure of merit for evaluating the performance of a fuel cell is the polarization curve, i.e., the fuel cell total potential as a function of current,

$$\widetilde{V}_i = \widetilde{V}_{i,\mathrm{a}} + \widetilde{V}_{i,\mathrm{c}} - \tilde{\eta}_{\mathrm{ohm}}. \tag{38}$$

The pumping power $\widetilde{W}_\mathrm{p}$ is required to supply the fuel cell with fuel and oxidant. Therefore the total net power (available for utilization) of the fuel cell is

$$\widetilde{W}_{\mathrm{net}} = \widetilde{W} - \widetilde{W}_\mathrm{p}, \tag{39}$$

where

$$\widetilde{W} = \widetilde{V}_i \tilde{I}, \tag{40}$$

$$\widetilde{W}_\mathrm{p} = \psi_\mathrm{f} S_\mathrm{f} \frac{\theta_1}{P_1} \Delta P_1 + \psi_{\mathrm{ox}} S_{\mathrm{ox}} \frac{\theta_7}{P_7} \Delta P_7, \tag{41}$$

$$S_i = \frac{\dot{m}_{\mathrm{ref}} T_\infty R_i}{V_{\mathrm{ref}} I_{\mathrm{ref}}}, \quad i = \mathrm{f}, \mathrm{ox}. \tag{42}$$

The objective function defined by Eq. (39) depends on the internal structure and the external shape of the fuel cell. The mathematical model allows the computation of the total net power of the fuel cell, $\widetilde{W}_{\mathrm{net}}$. This is possible to achieve as soon as the physical values (Table 1) and a set of geometric internal ($1 = 2\xi_\mathrm{b}/\xi_x + \sum_{i=1}^{7} \xi_i/\xi_x$) and external ($\xi_y/\xi_x$ and ξ_z/ξ_x) parameters are chosen for the overall system.

The maximum (theoretical) fuel cell efficiency is given by

$$\eta_i = \frac{\Delta\widetilde{G}_3 + \Delta\widetilde{G}_5}{\Delta\widetilde{H}_3 + \Delta\widetilde{H}_5}. \tag{43}$$

The actual first-law efficiency of the fuel cell is

$$\eta_\mathrm{I} = E \frac{\widetilde{W}}{\Delta\widetilde{H}_3 + \Delta\widetilde{H}_5}. \tag{44}$$

Table 1
Physical properties used as reference case in the numerical optimization of the overall system

$B = 0.156$ [28]	$q = 1.5$
$c_{p,\mathrm{f}} = 14.95\ \mathrm{kJ\,kg^{-1}\,K^{-1}}$	$R_\mathrm{f} = 4.157\ \mathrm{kJ\,kg^{-1}\,K^{-1}}$
$c_{p,\mathrm{ox}} = 0.91875\ \mathrm{kJ\,kg^{-1}\,K^{-1}}$	$R_{\mathrm{ox}} = 0.2598\ \mathrm{kJ\,kg^{-1}\,K^{-1}}$
$c_{\mathrm{v,f}} = 10.8\ \mathrm{kJ\,kg^{-1}\,K^{-1}}$	$T_\mathrm{f}, T_{\mathrm{ox}}, T_\infty = 298.15\ \mathrm{K}$
$c_{\mathrm{v,ox}} = 0.659375\ \mathrm{kJ\,kg^{-1}\,K^{-1}}$	$U_{wi} = 50\ \mathrm{W\,m^{-2}\,K^{-1}}$, $i = 1,7$
$i_{0,\mathrm{a}}, i_{0,\mathrm{c}} = 10\ \mathrm{A\,m^{-2}}$	$V_{\mathrm{ref}} = 1\ \mathrm{V}$
$I_{\mathrm{ref}} = 1\ \mathrm{A}$	$V_\mathrm{T} = 2.25 \times 10^{-5}\ \mathrm{m^3}$
$k_\mathrm{f} = 0.2\ \mathrm{W\,m^{-1}\,K^{-1}}$	$V_{\mathrm{T,ref}} = 10^{-5}\ \mathrm{m^3}$
$k_{\mathrm{ox}} = 0.033\ \mathrm{W\,m^{-1}\,K^{-1}}$	$\alpha_\mathrm{a}, \alpha_\mathrm{c} = 0.5$
$k_\mathrm{p} = 0.21\ \mathrm{W\,m^{-1}\,K^{-1}}$	$\mu_1 = 10^{-5}\ \mathrm{Pa\,s}$
$K_2, K_6 = 4 \times 10^{-14}\ \mathrm{m^2}$	$\mu_7 = 2.4 \times 10^{-5}\ \mathrm{Pa\,s}$
$K_3, K_5 = 4 \times 10^{-16}\ \mathrm{m^2}$	$\sigma_1, \sigma_7 = 1.388 \times 10^6\ \Omega^{-1}\,\mathrm{m^{-1}}$
$\dot{m}_{\mathrm{ref}} = 10^{-4}\ \mathrm{kg\,s^{-1}}$	$\sigma_2, \sigma_6 = 4000\ \Omega^{-1}\,\mathrm{m^{-1}}$
$p_\mathrm{f}, p_\infty = 0.1\ \mathrm{MPa}$	$\phi_2, \phi_6 = 0.4$
$p_{\mathrm{ox}} = 0.12\ \mathrm{MPa}$	$\phi_3, \phi_5 = 0.2$

where $E = V_{\mathrm{ref}} I_{\mathrm{ref}} / (\dot{m}_{\mathrm{ref}} c_{p,\mathrm{f}} T_\infty)$. The second-law efficiency is defined as the ratio of the actual electrical power to the reversible electrical power,

$$\eta_{\mathrm{II}} = E \frac{\widetilde{W}}{\Delta\widetilde{G}_3 + \Delta\widetilde{G}_5}. \tag{45}$$

The net efficiency of the fuel cell is

$$\eta_{\mathrm{net}} = E \frac{\widetilde{W}_{\mathrm{net}}}{\Delta\widetilde{H}_3 + \Delta\widetilde{H}_5}. \tag{46}$$

In a previous study, Vargas and Bejan [13] found the optimal distribution of the compartments shown in Fig. 1 for fuel cell maximum power under a volume constraint, for an alkaline fuel cell. However, the cross section area of the fuel cell was kept fixed in the process, therefore the external shape was not allowed to vary. In the present study, a PEM fuel cell is investigated, and the external shape of the cell is allowed to vary. Therefore, the optimization procedure starts by seeking the optimal internal structure of the fuel cell for a range of external shapes (ξ_y/ξ_x and ξ_z/ξ_x).

In the optimization procedure the total electrode wetted area varies. Because the total volume is fixed, the solution to the optimization problem is given directly in terms of net power and current, instead of power and current densities.

The optimization of internal structure is executed according to the lower part of Fig. 2. First, geometrical symmetry is assumed for the electrodes, i.e., the anode and cathode are assumed to have the same thickness. The thicknesses of the diffusion and reaction layers of the cathode and anode are varied simultaneously subject to fixed ratios of cathode thickness (y_2) and anode thickness (y_6) to total length,

$$\xi_2/\xi_x + \xi_3/\xi_x = y_2, \quad \xi_5/\xi_x + \xi_6/\xi_x = y_6. \tag{47}$$

The ratio of overall thickness to total length of the fuel cell is also fixed,

$$y_2 + y_4 + y_6 = 0.8. \tag{48}$$

Under the simplifying hypotheses assumed, the internal structure optimization problem is reduced to one degree of freedom, i.e., the ratio $\xi_3/\xi_x = \xi_5/\xi_x$. The end result is the optimized configuration of the fuel cell electrodes $(\xi_2, \xi_3, \xi_5, \xi_6)_{\mathrm{opt}}$, for which the net power is maximum.

Next the optimization focuses on the external shape. The optimized internal structure is kept fixed, i.e., ($1 = 2\xi_\mathrm{b}/\xi_x + \sum_{i=1}^{7} \xi_i/\xi_x$), and the external shape is varied in the process, i.e., (ξ_y/ξ_x and ξ_z/ξ_x). The objective is to find (ξ_y/ξ_x and $\xi_z/\xi_x)_{\mathrm{opt}}$ such that $\widetilde{W}_{\mathrm{net}}$ is maximum. The model constructed in Section 2 allows us to calculate the net power as a function of current, Eq. (39). The physical properties assumed in this calculation were suggested by previous studies and obtained from handbooks [6,8,9,20,26], and are listed in Table 1. Eqs. (4), (8), (10), (12), (20), (25), (27) and (28) form a system of nine algebraic equations. The unknowns are θ_i and P_i, i.e., the temperatures in the seven control volumes, and the gas pressures in CV2 and CV6. Once the temperatures and pressures are known, the electrical potentials and power can be calculated for an assumed current level.

Pressures are related to temperatures via Eq. (8). The system reduces to seven nonlinear algebraic equations, in which the unknowns are the temperatures of the seven control volumes. This system is solved using a quasi-Newton method [27]. For the cases studied in this paper, the Newton iterative process required approximately seven iterations to achieve convergence, such that the Euclidean norm of the residual of the system was less than 10^{-6}. Because of this, the computational time required for one steady-state solution was short.

4. Results and discussion

For the internal structure optimization, the maximum power is sought by optimizing the geometry as shown in the lower part of Fig. 2. For each investigated geometry, the net power is calculated by starting from open circuit ($\tilde{I} = 0$) and proceeding in increments of $\Delta\tilde{I} = 10$ until the net power is zero or the limiting current level is reached. This procedure is illustrated in Fig. 3, which shows simulation results for one selected geometric internal and external unit fuel cell configuration. The total and net power, and polarization curves are shown in Fig. 3a. According to the model, the actual open circuit voltage is equal to the reversible cell potential, because it has been assumed that no losses result from species crossover from one electrode through the electrolyte, and from internal currents. At low currents there is an accentuated potential drop due to activation polarization. This is followed by a region dominated by ohmic polarization. At high currents, close to the limiting current level, losses are due mainly to concentration polarization.

The total polarization is the sum of the electrical potential produced at the anode and cathode, $\widetilde{V}_{i,\mathrm{a}}$ and $\widetilde{V}_{i,\mathrm{c}}$. In a PEM fuel cell, the electrical potential produced at the anode is negative. Conversely, the electrical potential produced at the cathode is positive. The sum of such potentials minus the potential loss due to electrical resistance across the cell (ohmic loss) is the total fuel cell

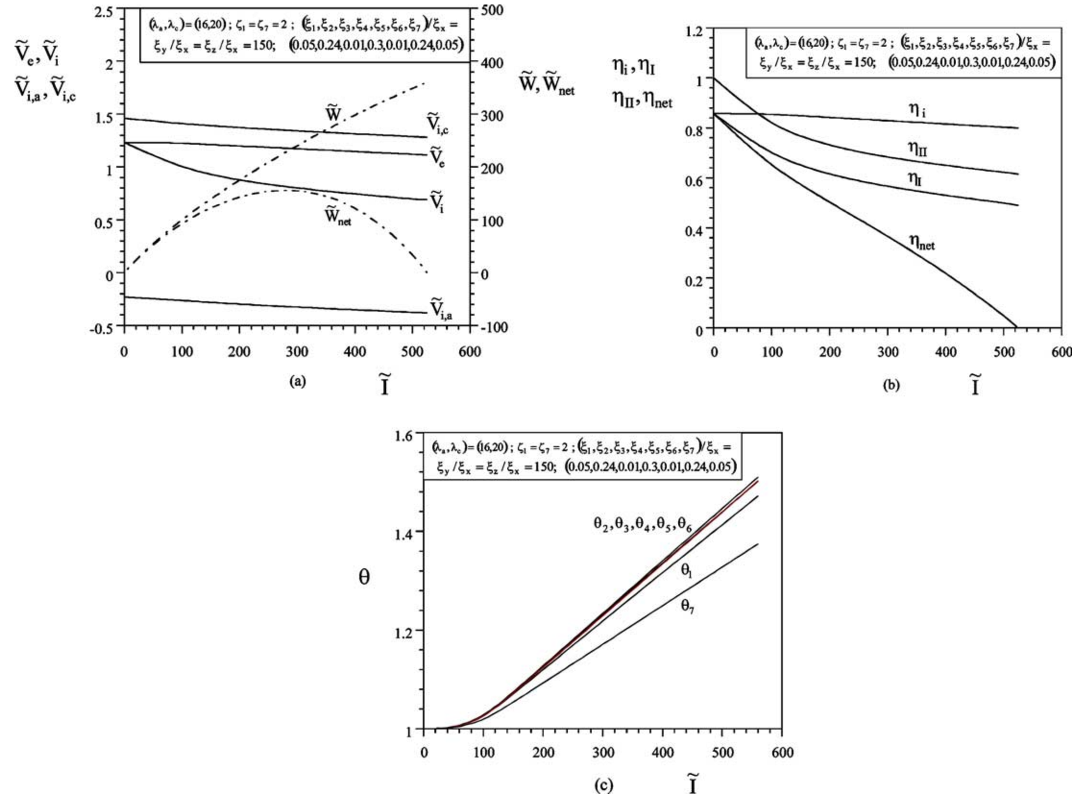

Fig. 3. (a) Example of polarization, total and net power output curves; (b) the ideal, first law, second law and net efficiencies for the PEM fuel cell considered in (a); and (c) the behavior of temperature versus current, for the PEM fuel cell considered in (a) and (b).

potential, $\widetilde{V}_i$. The change in the Gibbs free energy of reaction decreases as the temperature increases. Therefore, according to Eq. (15) the reversible electrical potential decreases as the temperature increases, what happens when the current increases. Furthermore, as the current increases the partial pressures of reactants at the catalyst layers decrease in accordance with Eq. (8), because fuel and oxidant consumption increase, eventually reaching the zero limit, where the voltage at the electrode drops to zero via the Nernst effect, Eq. (15).

In Fig. 3a, the simulation was conducted until $\widetilde{W}_{\text{net}} = 0$, i.e., up to the point where the electrical power produced by the fuel cell matched the required pumping power to supply fuel and oxidant at stoichiometric ratios $\zeta_1 = \zeta_7 = 2$. Under such selected operating conditions and geometry ($\xi_y/\xi_x = \xi_z/\xi_x = 150$), the fuel cell did not reach the concentration polarization region where either $\widetilde{V}_{i,\text{a}}$ or $\widetilde{V}_{i,\text{c}}$ would approach zero. The net power curve exhibits a maximum at $\widetilde{I} \approx 260$, which is central in the evaluation of global performance, by balancing total electrical power produced with required pumping power to supply fuel and oxidant to the fuel cell. The maximum net power is maximized during the optimization of geometry.

Fig. 3b shows that the ideal efficiency (η_i) decreases as the current increases. This effect is due to the temperature increase in the anode and cathode reaction layers. The temperature increase is captured by the present model. The first law efficiency is equal to the ideal efficiency at open circuit ($\widetilde{I} = 0$), and decrease monotonically as the current increases. The second law efficiency is equal to 1 (reversible operation—no losses) at open circuit ($\widetilde{I} = 0$), and also decrease monotonically as the current increases. The net efficiency behavior shows the effect of increasing current and therefore pressure drop in the gas channels, i.e., the pumping power increases and the net power decreases, reaching a zero limit when $\widetilde{W}_{\text{net}} = 0$.

The fuel flow rate increases as the current increases, Eq. (5), therefore more heat is generated by the reactions at the anode and cathode, and the temperature increases. The temperatures in the fuel cell compartments shown in Fig. 1 increase as current increases, as shown in Fig. 3c, since more heat is generated by the electrochemical reaction and by Joule effect (ohmic heating). The higher the current, the more accentuated are the temperature spatial gradients between the fuel cell compartments, even for the unit fuel cell considered in Fig. 3, with the selected high geometric aspect ratio of $\xi_y/\xi_x = \xi_z/\xi_x = 150$, i.e., with a small thickness compared to width and height. Furtherly, since hydrogen is roughly ten times more thermally conductive than oxygen, the temperatures in the gas channels are considerably different, which is also captured by the model. Therefore, the fuel cell power and polarization curves produced by the present model take into account all internal spatial temperature gradients, which directly affect the polarization curve and, therefore the total electrical power output.

Fig. 4a illustrates the optimization of internal structure: the maximization of net power by varying $\xi_3/\xi_x = \xi_5/\xi_x$ subject to fixed y_2 and y_6, which also means that the membrane thickness is fixed, i.e., $y_2 + y_4 + y_6 = 0.8$ (Fig. 2). The optimal allocation of thickness results from the trade-off between two effects: activation polarization losses and ohmic losses. As ξ_3/ξ_x and ξ_5/ξ_x increase, the electrode wetted areas increase and the activation losses decrease. On the other hand, the ohmic losses increase because the ionomer penetrates deeper into the electrodes, increasing electrical resistance. Another interesting phenomenon is that the ionomer electrical conductive increases as temperature increases at higher current levels, and with water content increase as well, therefore reducing ohmic loss at higher temperatures, which is represented by Eq. (21). The results of those trade-offs observed during internal geometry variation in the optimization process is investigated in Fig. 4a which shows net power maxima for two fuel cell external geometric aspect ratios and ionomer water contents. The internal structure optimization was performed for given stoichiometric ratios, two values of the unit fuel cell external aspect ratio $\xi_y/\xi_x = \xi_z/\xi_x$, i.e., 30 and 50, for two different ionomer water content conditions, i.e., $(\lambda_\text{a}, \lambda_\text{c}) = (10, 14)$ and $(\lambda_\text{a}, \lambda_\text{c}) = (16, 20)$. At higher ionomer water content the maximum fuel cell net power is higher, mainly due to the fact that ionomer electrical conductivity increases with water content and, therefore ohmic losses decrease. An important observation is that the optimal internal structure, represented by $(\xi_3/\xi_x = \xi_5/\xi_x)_{\text{opt}}$, did not vary with the variation of the external shape $\xi_y/\xi_x = \xi_z/\xi_x$ for a particular water content.

The results of the internal structure optimization with respect to the average membrane water content, $\lambda = (\lambda_\text{a} + \lambda_\text{c})/2$, are shown in Fig. 4b, for different external shapes $\xi_y/\xi_x = \xi_z/\xi_x$. The optimal internal structure, represented by $(\xi_3/\xi_x = \xi_5/\xi_x)_{\text{opt}}$, is independent of external shape for all tested water contents. As $\xi_y/\xi_x = \xi_z/\xi_x$ increases the net power maximized with respect to $\xi_3/\xi_x = \xi_5/\xi_x$, $\widetilde{W}_{\text{net,m}}$, increases. The same effect is also observed as the water content increases, mainly due to smaller ohmic losses at higher water contents, as discussed in the previous paragraph.

The main conclusion at this point is that $(\xi_3/\xi_x = \xi_5/\xi_x)_{\text{opt}}$ is nearly the same in Fig. 4b for all tested membrane water contents and external shapes, meaning that the optimal internal structure is relatively insensitive to changes in both λ and $\xi_y/\xi_x = \xi_z/\xi_x$. This is important to proceed to the fuel cell external shape optimization, which is illustrated in Fig. 5. Based on the observation that the optimized inner parameters (ξ_3/ξ_x, $\xi_5/\xi_x \cong 0.01$) are practically insensitive, i.e., "robust" to changes in the external shape, the fuel cell external shape

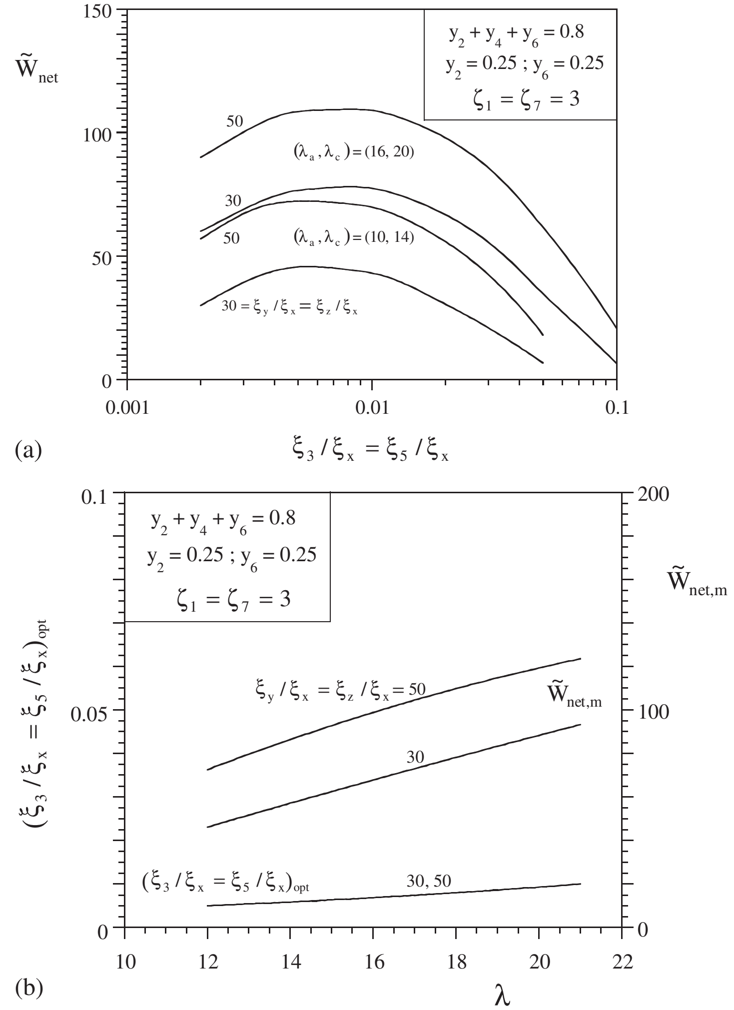

Fig. 4. (a) The internal structure optimization according to Fig. 2 and the dependence on external shape and ionomer water content for $\zeta_1 = \zeta_7 = 3$, and (b) the results of the internal structure optimization with respect to average membrane water content, λ, for $\zeta_1 = \zeta_7 = 3$, and their dependence on external shape.

optimization procedure is therefore conducted for a fixed internal shape structure defined by $(\xi_3/\xi_x = \xi_5/\xi_x)_{\text{opt}} = 0.01$.

Taken together, the results of Figs. 3 and 4 document the performance and the optimized internal architecture of a unit fuel cell over a range of external parameters. These results hold for the reference properties listed in Table 1, where the total volume was set at $V_T = 2.25 \times 10^{-5}$ m^3. For the convenience of presenting dimensionless results and recognizing the fuel cell net power varies with size (total volume), a dimensionless fuel cell total volume is defined as $\tilde{V}_T = V_T/V_{T,\text{ref}}$, where a reference total volume was set at $V_{T,\text{ref}} = 10^{-5}$ m^3 also in Table 1.

Fig. 5a shows that for the optimized internal structure, and a given ionomer water content, the once maximized fuel cell net power with respect to internal structure ($\tilde{W}_{\text{net,m}}$) can be maximized with respect to external shape under a fixed volume constraint, i.e., $\tilde{V}_T = 2.25$. The occurrence of a net power maximum with respect to fuel cell external shape is explained by analyzing two extremes: (i) small $\xi_y/\xi_x = \xi_z/\xi_x$ implies that ξ_x is large, $\tilde{W}$ is small due to large flow resistances in the x-direction, and $\tilde{W}_p$ is small due to a small swept length ξ_z, therefore $\tilde{W}_{\text{net,m}} \to 0$, and (ii) large $\xi_y/\xi_x = \xi_z/\xi_x$ implies that ξ_x is small, $\tilde{W}$ is large due to small flow resistances in the x-direction and also large wetted areas at the electrodes, but $\tilde{W}_p$ is also large due to a large swept length ξ_z and small hydraulic diameters D_h, therefore $\tilde{W}_{\text{net,m}} \to 0$ at this extreme too. Hence, there must exist an intermediate and optimal $\xi_y/\xi_x = \xi_z/\xi_x$

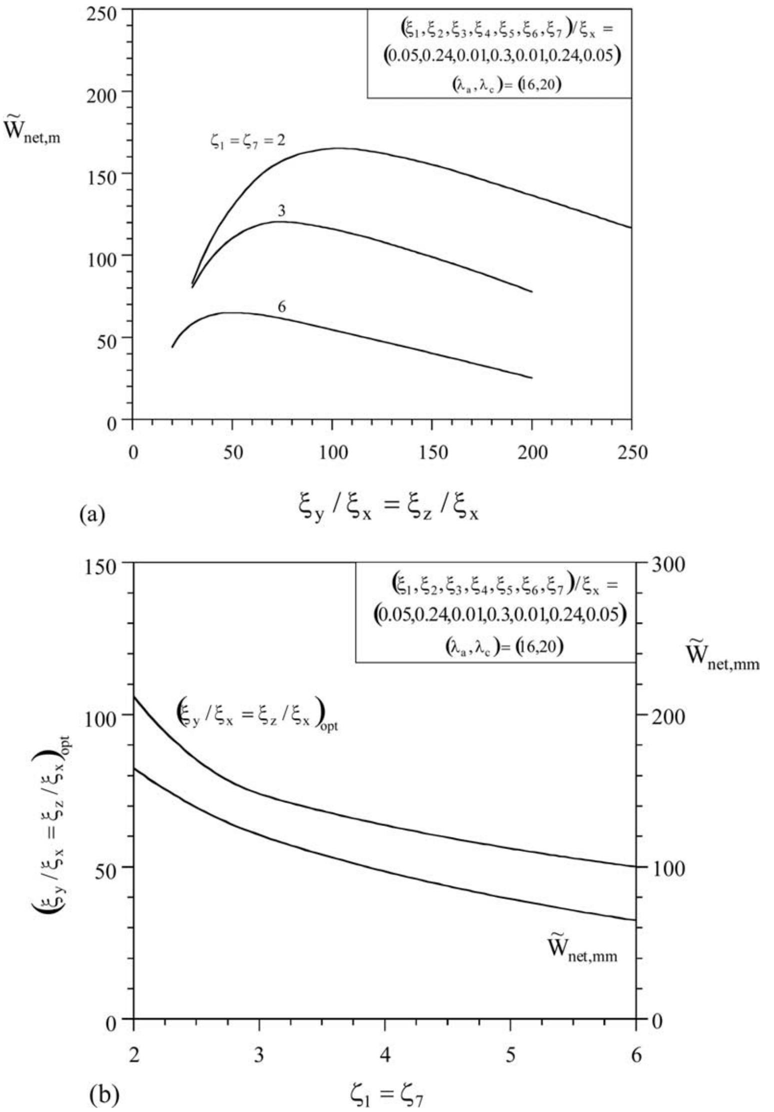

Fig. 5. (a) The external structure optimization and the dependence on stoichiometric ratio for $(\lambda_a, \lambda_c) = (16, 20)$, and (b) the results of the external structure optimization with respect to the stoichiometric ratios, $\zeta_1 = \zeta_7$, for $(\lambda_a, \lambda_c) = (16, 20)$.

geometric configuration such that $\widetilde{W}_{net,m}$ is maximum, which balances the trade-off between electrical power output and pumping power to supply fuel and oxidant to the fuel cell according to Eq. (39).

The fuel cell net power is plotted in Fig. 5a as a function of $\xi_y/\xi_x = \xi_z/\xi_x$ for three different stoichiometric ratios regimes, $\zeta_1 = \zeta_7$. For all stoichiometric ratios, a maximum net power, $\widetilde{W}_{net,mm}$, is observed, determining the optimal external fuel cell structure, represented by $(\xi_y/\xi_x = \xi_z/\xi_x)_{opt}$. As the stoichiometric ratios increase, the net power decreases, since the fuel and oxidant mass flow rates in the gas channels increase, and therefore pressure drops and pumping power increase.

The optimization results of Fig. 5a are plotted in Fig. 5b as functions of the stoichiometric ratios. Both $\widetilde{W}_{net,mm}$ and $(\xi_y/\xi_x = \xi_z/\xi_x)_{opt}$ decrease monotonically as the stoichiometric ratios increase. The reason for that is that as the stoichiometric ratios increase the pumping power increases as well, therefore the optimal external geometry defined by $(\xi_y/\xi_x = \xi_z/\xi_x)_{opt}$ shows smaller values such that the swept lengths in the gas channels decrease and hydraulic diameters increase, therefore reducing pressure drops and pumping power.

In a subsequent phase of this study, the volume constraint $\widetilde{V}_T = 2.25$ was relaxed, and $\widetilde{V}_T$ was varied over the range 1–10, for stoichiometric ratios $\zeta_1 = \zeta_7 = 2$. This variation is indicated by the three curves of Fig. 6a.

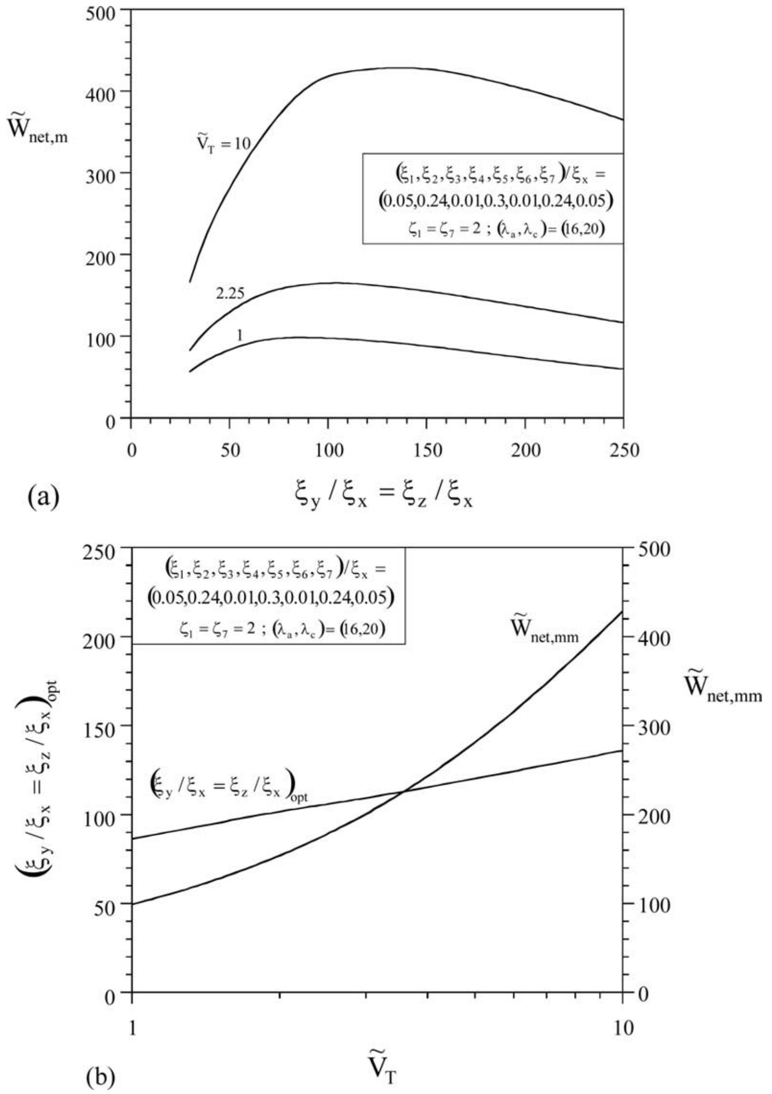

Fig. 6. (a) The external structure optimization and the dependence on total fuel cell volume, for $\zeta_1 = \zeta_7 = 2$ and $(\lambda_a, \lambda_c) = (16, 20)$, and (b) the results of the external structure optimization with respect to total fuel cell volume, $\widetilde{V}_T$, for $\zeta_1 = \zeta_7 = 2$ and $(\lambda_a, \lambda_c) = (16, 20)$.

For that, two additional values of $\widetilde{V}_T$, i.e., 1 and 10 were investigated and the results plotted together with the previously obtained results for $\widetilde{V}_T = 2.25$. The three resulting curves exhibit maxima with respect to the external shape aspect ratios. The fuel cell net power increases as $\widetilde{V}_T$ increases. Additional results were produced to cover the entire range $1 \leqslant \widetilde{V}_T \leqslant 10$, which allowed the twice maximized net power and the optimized external shape aspect ratios to be plotted in Fig. 6b as functions of $\widetilde{V}_T$. The twice maximized net power increases monotonically with total volume. The optimized external shape aspect ratios also increase as the fuel cell total volume increases, but at a smaller rate, staying approximately within the range $90 \leqslant (\xi_y/\xi_x = \xi_z/\xi_x)_{opt} \leqslant 130$. So, for the investigated total volume range, the optimized external shape is therefore $(\xi_y/\xi_x = \xi_z/\xi_x)_{opt} \cong 100$.

5. Conclusions

In this paper we showed that the internal and external structure of a PEM fuel cell can be optimized so that the net power is maximized. We demonstrated this at the most elemental level, by constructing a model for fluid flow, mass and heat transfer in a unit PEM fuel cell, which takes into account spatial temperature and pressure gradients (Fig. 1). The internal structure has an optimal allocation such that wetted area in the reaction layers and electrical resistance are optimally balanced for maximum electrical power. Additionally, a three-dimensional flow space with the dimensions L_z and L_y in the plane perpendicular to L_x was considered and the total volume was fixed. The new degrees of freedom, i.e., the aspect ratios L_y/L_x and L_z/L_x, allowed for the optimization of the system external shape, in addition to the internal structure. As a result, it was also found an external shape defined by dimensionless external geometric aspect ratios, ξ_y/ξ_x and ξ_z/ξ_x, such that electrical and pumping power are optimally balanced for maximum net power. All optimization results were presented non-dimensionally for the sake of generality.

Conceptually, we showed that trade-offs exist, and that from them results the internal structure and external shape—the relative sizes and spacings—of flow systems, i.e., constructal design [5,13]. In practice, such trade-offs must be pursued based on models that correspond to real applications. Based even on the simplified model used in this paper, it is evident that significant optima exist, and must be identified accurately. The current optimization results reported in this study, clearly demonstrate that even for a unit PEM fuel cell, gas supply causes pressure drops that induce considerable power consumption that need to be taken into account in fuel cell design.

The main conclusion is that constructal optimization procedure needs to be implemented to optimize thermal and water management, and the flowfield design, which will lead to the best internal and external shape of a fuel cell stack for maximum power density and/or efficiency. In general, the flowfield should be designed to minimize pressure drop (reducing parasitic pump requirements), while providing adequate and evenly distributed mass transfer through the carbon diffusion layer to the catalyst surface for reaction. The fuel cell stack needs to be optimally "constructed" from its smallest (elemental) scale, i.e., the unit fuel cell, as shown in Fig. 1. Instead of the conventional serpentine, parallel and interdigitated flow configurations utilized in current fuel cell stacks [1], it is expected that constructal optimization will lead to high-density constructions with new scaling laws that are dictated by dendritic (space-filling, fractal-like) flow structures.

Acknowledgements

The authors acknowledge with gratitude the support of the Center for Advanced Power Systems at Florida State University, and the Program of Human Resources for the Oil Sector and Natural Gas, of the Brazilian Oil National Agency—PRH-ANP/MCT.

References

[1] M.M. Mench, C. Wang, S.T. Thynell, An introduction to fuel cells and related transport phenomena, Int. J. Trans. Phenom. 3 (2001) 151–176.

[2] P.F. Howard, C.J. Greenhill, Ballard PEM fuel cell powered ZEV bus, Society of Automotive Engineers, SAE, 1993, Paper 931817.

[3] U. Cantoni, Alternative fuels utilization in fuel cells for transportation, Society of Automotive Engineers, SAE, 1993, Paper 931816.

[4] D. Linden, Handbook of Batteries and Fuel Cells, McGraw-Hill, New York, 1984.

[5] A. Bejan, Shape and Structure, from Engineering to Nature, Cambridge University Press, Cambridge, UK, 2000.

[6] T.E. Springer, T.A. Zawodzinski, S. Gottesfeld, Polymer electrolyte fuel cell model, J. Electrochem. Soc. 138 (8) (1991) 2334–2341.

[7] S.F. Baxter, V.S. Battaglia, R.E. White, Methanol fuel cell model: anode, J. Electrochem. Soc. 146 (1999) 437–447.

[8] V. Gurau, F. Barbir, H. Liu, An analytical solution of a half-cell model for PEM fuel cells, J. Electrochem. Soc. 147 (2000) 2468–2477.

[9] A.A. Kulikovsky, J. Divisek, A.A. Kornyshev, Two-dimensional simulation of direct methanol fuel cells—a new (embedded) type of current collector, J. Electrochem. Soc. 147 (2000) 953–959.

[10] T. Thampan, S. Malhotra, H. Tang, R. Datta, Modeling of conductive transport in proton-exchange membranes for fuel cells, J. Electrochem. Soc. 147 (2000) 3242–3250.

[11] L. Pisani, G. Murgia, M. Valentini, B. D'Aguanno, A working model of polymer electrolyte fuel cells—comparisons between theory and experiments, J. Electrochem. Soc. 149 (7) (2002) A898–A904.

[12] T. Zhou, H. Liu, A general three-dimensional model for proton exchange membrane fuel cells, Int. J. Trans. Phenom. 3 (2001) 177–198.

[13] J.V.C. Vargas, A. Bejan, Thermodynamic optimization of internal structure in a fuel cell, Int. J. Energy Res. 28 (4) (2004) 319–339.

[14] R.B. Bird, W.E. Stewart, E.N. Lightfoot, Transport Phenomena, second ed., Wiley, New York, 2002.

[15] J.S. Newman, Electrochemical Systems, second ed., Prentice Hall, Englewood Cliffs, NJ, 1991, pp. 255, 299, 461.

[16] J.A. Wesselingh, P. Vonk, G. Kraaijeveld, Exploring the Maxwell–Stefan description of ion-exchange, Chem. Eng. J. Biochem. Eng. J. 57 (1995) 75–89.

[17] M.J. Moran, R. Shapiro, Fundamentals of Engineering Thermodynamics, third ed., Wiley, New York, 1993.

[18] W.L. Masterton, C.N. Hurley, Chemistry Principles & Reactions, third ed., Saunders College Publishing, Orlando, FL, 1997.

[19] T.A. Zawodzinski, M. Neeman, L.O. Sillerud, S. Gottesfeld, Determination of water diffusion-coefficients in perfluorosulfonate ionomeric membranes, J. Phys. Chem. 95 (15) (1991) 6040–6044.

[20] J.O'M. Bockris, D.M. Drazic, Electro-chemical Science, Taylor and Francis, London, 1972.

[21] A.J. Bard, L.R. Faulkner, Electrochemical Methods—Fundamentals and Applications, second ed., Wiley, New York, 2001.

[22] G. Li, P.G. Pickup, Ionic conductivity of PEMFC electrodes, J. Electrochem. Soc. 150 (11) (2003) C745–C752.
[23] A.P. Saab, F.H. Garzon, T.A. Zawodzinski, Determination of ionic and electronic resistivities in carbon/polyelectrolyte fuel-cell composite electrodes, J. Electrochem. Soc. 149 (12) (2002) A1541–A1546.
[24] R.K. Shah, A.L. London, Laminar Flow Forced Convection in Ducts, Supplement 1 to Advances in Heat Transfer, Academic Press, New York, 1978.
[25] A. Bejan, Convection Heat Transfer, second ed., Wiley, New York, 1995 (Chapter 8).
[26] D.R. Lide (Ed.), CRC Handbook of Chemistry and Physics, 83rd ed., CRC Press, Boca Raton, FL, 2002/2003.
[27] D. Kincaid, W. Cheney, Numerical Analysis Mathematics of Scientific Computing, first ed., Wadsworth, Belmont, CA, 1991.
[28] M.R. Tarasevich, A. Sadkowski, E. Yeager, in: B.E. Convay, J.O'M. Bockris, E. Yeager, S.U.M. Khan, R.E. White (Eds.), Comprehensive Treatise of Electrochemistry, vol. 7, Plenum, New York, 1983, pp. 310–398.